Mitochondrial Localization and the Persistent Migration of Epithelial Cancer cells

Salil P. Desai,[†‡] Sangeeta N. Bhatia,[†§] Mehmet Toner,[†‡] and Daniel Irimia[‡*]

[†]Harvard-MIT Division of Health-Science Technology, Massachusetts Institute of Technology, Cambridge, Massachusetts; [‡]Department of Surgery, Massachusetts General Hospital, Harvard Medical School, Boston, Massachusetts; and [§]Howard Hughes Medical Institute, Chevy Chase, Maryland

ABSTRACT During cancer cell invasion, faster moving cancer cells play a dominant role by invading further and metastasizing earlier. Despite the importance of these outlier cells, the source of heterogeneity in their migratory behavior remains poorly understood. Here, we show that anterior localization of mitochondria, in between the nucleus and the leading edge of migrating epithelial cancer cells, correlates with faster migration velocities and increased directional persistence. The asymmetry of mitochondrial localization along the axis of migration is absent during spontaneous cell migration on two-dimensional surfaces and only occurs in the presence of chemical attractant cues or in conditions of mechanical confinement. Moreover, perturbing the asymmetric distribution of mitochondria within migrating cells by interfering with mitochondrial fusion (opa-1) or fission (drp-1) proteins, significantly reduces the number of cells with anterior localization of mitochondria and significantly decreases the velocity and directional persistence of the fastest moving cells. We also observed similar changes after perturbing the linkage between mitochondria and microtubules by the knockdown of mitochondrial rhoGTPase-1 (miro-1). Taken together, the changes in migration velocity and directional persistence in cells with anterior-localized mitochondria could account for an order of magnitude differences in invasive abilities between cells from otherwise homogenous cell populations.

INTRODUCTION

Longitudinal asymmetry of signals and cellular structures along the axis of migration is an important characteristic of motile epithelial cells. Several intracellular signals are differentially activated at the leading and trailing edges of migrating cells. These signals drive preferential activation of small GTPases Rho and Cdc42 at the leading (anterior) edge and Rac and PTEN toward the trailing (posterior) edge (1). Cytoskeletal components and organelles are also segregated along the axis of cell migration. Actin polymerization and the formation of new focal adhesions occur in the direction of movement at the leading edge, whereas actomyosin contraction and focal adhesion release are localized to the trailing edge. The microtubule organization complex is often localized between the nucleus and leading edge (2) and the endoplasmic reticulum and Golgi apparatus also occupy similar anterior positions (3,4). Whether the specific localizations of these organelles confer distinct migratory behaviors, however, remains elusive (5). In lymphocytes, mitochondrial localization is observed between the nucleus and the trailing edge of the cell during chemokine-induced migration (6), and has been shown to confer enhanced migratory properties such as increased persistence of migration in a specific direction. The highly dynamic nature of mitochondrial networks in eukaryotic cells (7) is evidence of their ability to organize within the cytosol to power cellular processes. Live-cell imaging has revealed that these networks are highly dynamic even at the level of individual organelles—with individual mitochondria stopping, starting, and changing direction (8). Individual mitochondrial transport has been studied extensively in neuronal cells (9) and mitochondrial content in neuronal processes correlates closely with the high energy demand in these structures needed to generate action potentials (10). Such purposeful localization of mitochondria has important implications in propagating growth cones in neuronal cells and in driving cell migration in lymphocytic cells. However, the redistribution of mitochondria within motile cancer cells has been largely unexplored.

Cancer cells migrating away from the primary tumor are ultimately responsible for the formation of distant metastasis and the death of 90% of cancer patients. Although the role of cancer cell migration in disease progression has been investigated both in vivo (11–13) and in vitro (14–16), a migration-based quantifier for the disease state has remained elusive. Among the hallmarks that define the aggressiveness of various cancers (17), the ability of cells to migrate holds a secondary role. One of the difficulties in assessing the role of cell migration is the fact that the migration phenotype of cancer cells is highly heterogeneous even within the same tumor (18,19). Importantly, recently developed tools for detailed characterization of the cancer cell migration phenotype (20,21) quantify fundamental characteristics of motility—velocity, persistence, and directionality at the level of individual cells. Leveraging such tools enables us to explore the heterogeneity of the motility phenotype of cancer cells and its associations with other processes involved in epithelial cancer cell migration.

Here, we show that strong correlations exist between the localization of mitochondria within moving cells and

Submitted May 22, 2012, and accepted for publication March 7, 2013.

*Correspondence: dirimia@hms.harvard.edu

Editor: Alissa Weaver.

0006-3495/13/05/2077/12 $2.00

http://dx.doi.org/10.1016/j.bpj.2013.03.025

their speed and directional persistence during migration. To observe these correlations, we engineered various complex microenvironments involving both mechanical and biochemical cues to precisely quantify speed and persistence during migration in epithelial cancer cells with single-cell resolution. We designed and implemented several microfluidic platforms that provided a range of mechanical confinements (from channels with a varying cross-sectional area to completely unconstrained environments) and the ability to apply superimposed chemotactic gradients within these confinements. Furthermore, we observed that the speed and persistence during cell migration were significantly reduced after altering intracellular mitochondrial relocalization processes through mutations in mitochondrial shaping proteins or proteins participating in mitochondrial transport. Elucidating the coupling between mitochondrial localization and cancer cell migration in various microenvironments could shed light on the role of mitochondrial dynamics in cancer progression and provide the first steps to identifying and targeting highly migratory phenotypes in epithelial cancer cells.

MATERIALS AND METHODS

Cell culture

MDA-MB-231, MDA-MB-435, and PC3 cell lines were obtained from the ATCC. The PC3M cell line was provided courtesy of the Lindquist Lab. Cells are cultured, as recommended by ATCC, in appropriate media supplemented with 10% (v/v) fetal bovine serum and 2% (v/v) penicillin-streptomycin (for details, see the Supporting Material). For imaging and visualization, cells were labeled with nuclear-staining Hoechst (Invitrogen, Carlsbad, CA) and mitochondrial staining MitoTracker Red (Invitrogen) dyes (for details, see the Supporting Material).

Mutagenesis

Mutant versions of mitochondrial shaping proteins, fission (drp-1) and fusion (opa-1), were generated using standard site-directed mutagenesis techniques (for details, see the Supporting Material and Fig. S1). Cells constitutively expressing enhanced green fluorescence protein were sorted for positive expression. Sorted cells cultured in 96-well plates, single-cell per well, were further sorted under a selection pressure of 500 μg/ml geneticin. Five clones were picked and further expanded for two cell passages and used for experiments. Knockdowns of mitochondrial rhoGTPase (miro/rhot-1) were generated using lentiviral constructs provided by the RNAi Consortium (TRC) (for details, see the Supporting Material).

ATP assays

Cellular lysates from ~1 $\times$ 10^6 cells were collected for measurement of intracellular ATP content. ATP content was determined using a bioluminescence detection kit (ENLITEN, Promega, Madison, WI) according to the manufacturer's instructions (for details, see the Supporting Material.

Image acquisition and analysis

Migrating cells were imaged using a Nikon (Tokyo, Japan) TiE microscope equipped with an incubation chamber. Time-lapse images were acquired at multiple spatial locations and multiple wavelengths every 15 or 20 min, and analyzed using custom MATLAB (The MathWorks, Natick, MA) scripts (for details, see the Supporting Material). The persistence of migration was quantified by determining the ratio of the shortest, linear distance from the starting point to the end point and the total distance traversed by the cell, as previously described (22). To assess mitochondrial localization within cells, mitochondria and the nucleus were fluorescently labeled as described previously. The centroid of the nucleus was used to mark the center of the cell. Line scans of mitochondrial fluorescence were integrated before and after the center of the cell. A mitochondrial localization (MLI) index was calculated as the ratio between the integrated area of the fore and the extent of the fore and aft spatial regions. MLI >0.65 was scored as anterior localized, <0.35 was scored as posterior localized, and between 0.35 and 0.65 was scored as unlocalized. Additional details and imaging protocols are described in the Supporting Material and Fig. S2.

Device microfabrication

Microfluidic devices of three distinct designs were implemented using standard multilayer soft lithography techniques. To observe the spontaneous migration of epithelial cells, microfluidic devices consisted in arrays of 6 μm tall and between 6 and 25 μm wide channels, connecting 50 μm tall cell and external chambers, as previously described (23). In some devices, the cross section of the channels varied between 6 $\times$ 6 and 6 $\times$ 25 μm. To observe the migration of epithelial cells in stable growth factor gradients and conditions of mechanical confinement, multilayered devices with migration channels and valves were manufactured as previously described (24). Finally, to observe the migration of cells in response to stable growth factor gradients, devices were fabricated combining migration channels and closed side chambers, as recently described in detail (25). Additional details regarding the device manufacturing, surface preparation, and experimental setup are presented in the Supporting Material.

Statistical analysis

Pearson sample correlation coefficients between velocity and MLI (r_v), and persistence and MLI (r_p) were computed using MATLAB (The MathWorks, Natick, MA). Best fit lines in all scatter plots were calculated by linear regressions in MATLAB. Normalized slopes (m) and least-squares errors (R^2) were extracted from fitting functions. Statistical significance between binned populations of anterior, posterior, and unlocalized cells (see Fig. 3, *C* and *E)* were performed using Student's *t*-test, where *p*-values of $p < 0.05$ were considered statistically significant. Error bars were generated for experiments performed in triplicate by representing one standard deviation from the mean.

RESULTS

Mitochondrial localization during spontaneous migration

Breast epithelial carcinoma cells (MDA-MB-231) cells migrated spontaneously on flat, two-dimensional surfaces and showed specific localizations of mitochondria without correlation with speed or persistence. Mitochondrial localizations were determined by identifying nuclear centroids (*yellow circles* in Fig. 1 *A*) and calculating the axis of migration—regions anterior to and posterior to the nucleus define the two cellular compartments (labeled respectively as A and P in Fig. 1 *A*). Mitochondria localizations, quantified by the MLI, were calculated at specific instants in time (Fig. 1 *B*). During random migration on a flat surface,

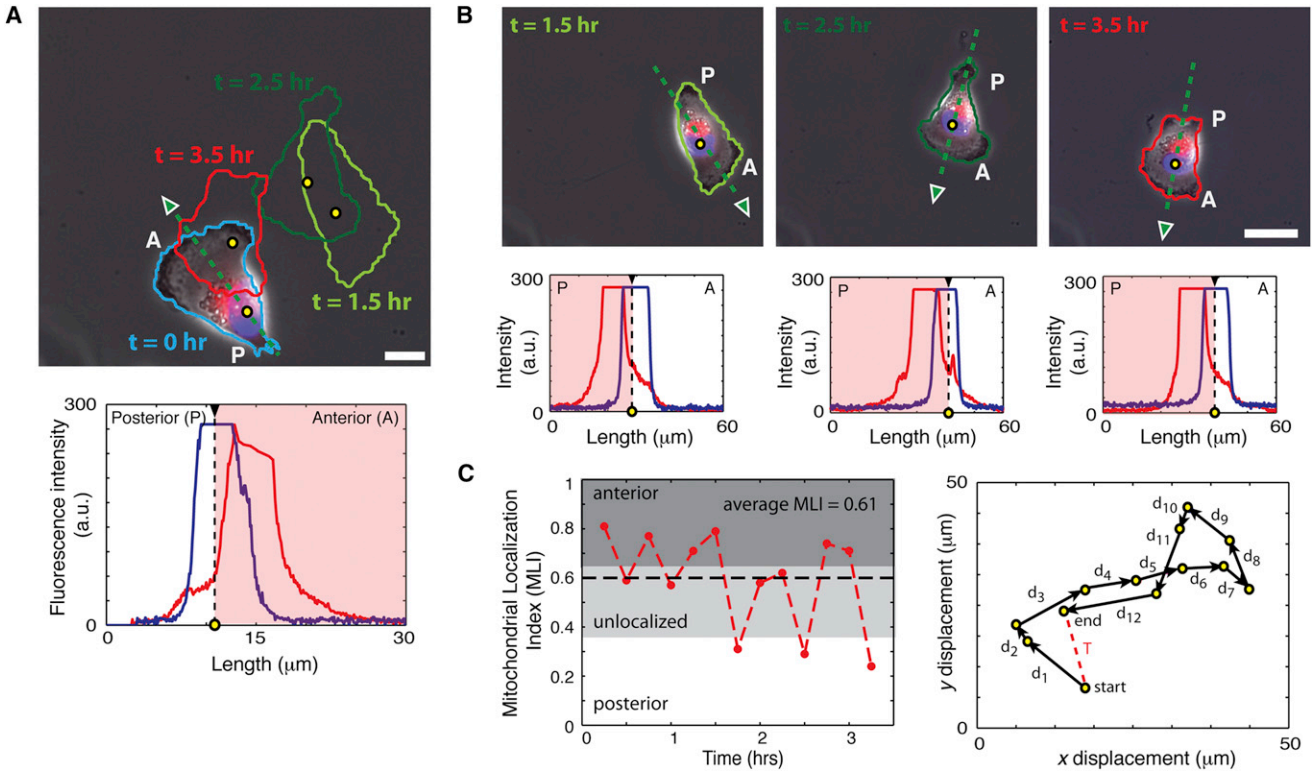

FIGURE 1 Mitochondrial localization during the spontaneous migration of the epithelial cancer cell in unconstrained environments. (*A*) Composite image of a single breast cancer cell (MDA-MB-231) with outlines/centroids showing the time course of unconstrained, spontaneous migration on a two-dimensional surface. Yellow dots indicate centroids and green arrowheads indicate direction of migration. P and A denote posterior and anterior regions of a migrating cell, respectively. Scale bar 10 μm. Line scans (*green dashed line*) show snapshot of localization (*plot*) with mitochondrial (*red*) and nuclear (*blue*) fluorescence intensities with mitochondria localized anterior to the nucleus. (*B*) Single cells from representative time points showing varying mitochondrial localizations. Scale bar 15 μm. (*C*) Left panel, time trace of instantaneous MLI (*red line trace*) of a single cell and average MLI (0.61) shown as a dashed line. Right panel, vector map of single cell traveling between nuclear centroid positions (*yellow dots*). Distances traversed between time points are labeled as $d_{time\ point}$. Dashed red line labeled T denotes shortest distance between start and end positions.

instantaneous MLI oscillated around a mean value of 0.6 (Fig. 1 *C*, *left panel*) and cells showed a low degree of persistence, as evidenced by trajectories across time (Fig. 1 *C*, *right panel*).

Mitochondrial localization during chemotaxis in biochemical gradients

MDA-MB-231 cells migrating in a gradient of epidermal growth factor (100 ng/ml EGF) showed predominantly anterior mitochondrial localization (Fig. 2 *A*, *left panel*). MLI increased progressively during exposure to EGF gradients in cells that moved toward a high concentration of chemoattractant (Fig. 2 *A*, *right panel*). During unconstrained migration in biochemical gradients approximately seven times more cells displayed anterior-localized mitochondria compared with cells migrating in the absence of gradients. Importantly, higher Pearson correlation coefficients exist between MLI and velocity and persistence ($r_v = 0.68$ and $r_p = 0.70$, respectively) than for cells migrating in a gradient than in the absence of gradients ($r_v = 0.63$ and $r_p = 0.61$), as summarized in Fig. 2 *B*. Similar observations were made with MCF7 breast adenocarcinoma cells migrating in 100 ng/ml insulin-like growth factor gradients and these results are summarized in Fig. S3.

Mitochondrial localization during migration in confined spaces

To measure the speed and persistence more precisely and for larger numbers of cells, we employed microscale channels within which epithelial cells migrate persistently at a constant speed for longer periods of time (20) in self-generated guiding EGF gradients (21). We found that mitochondria were localized predominantly in the anterior position within cells migrating spontaneously through 6 × 6 μm cross-section channels (Fig. 3 *A*, Movie S1). Three-dimensional rendering using confocal microscopy of the cells confirmed that two-dimensional images of localized mitochondria are an accurate representation of mitochondrial distribution (Fig. 3 *A*, *right panel*). Additionally, we found that cells with the most asymmetric distribution of mitochondria toward the anterior—higher MLI—are also the fastest moving and the most persistent (Fig. 3 *B*). Spontaneously migrating

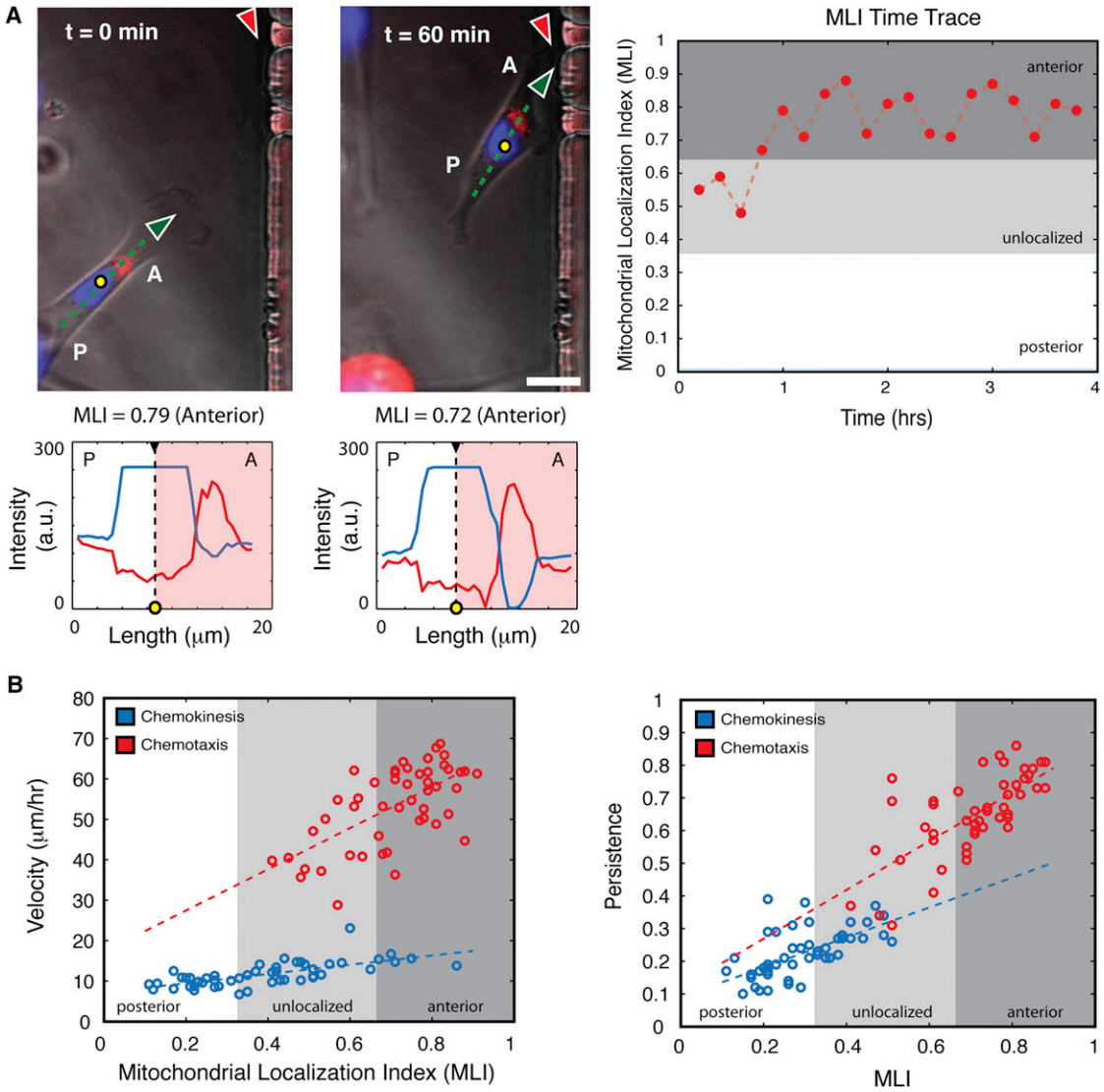

FIGURE 2 Mitochondrial localization during the migration of the epithelial cancer cell in unconstrained environments in the presence of biochemical gradients. (*A*) Image of a single breast cancer cell showing distinct anterior localization in a gradient (*red arrowheads* show location of chemokine source). Yellow dots indicate centroids and green arrowheads indicate direction of migration. Anterior and posterior regions are denoted as A and P. Scale bar 10 μm. Lower panel shows line scans of fluorescence (along *dashed green line*) indicating anterior localizations. Right panel shows a representative time trace of MLI showing a transient before the cell settles into a sustained anterior localization of mitochondria. (*B*) During unconstrained migration in the presence of biochemical gradients significant correlations exist between MLI and velocity (m = 0.64, $R^2 = 0.40$), and between MLI and persistence (m = 0.75, $R^2 = 0.49$). During spontaneous, unconstrained migration in the absence of gradients the correlations between MLI and average velocity (*left panel*, *blue dashed line*, m = 0.14, $R^2 = 0.47$) and persistence (*right panel*, *blue dashed line*, m = 0.45, $R^2 = 0.38$).

cells showed high correlations with both velocity and MLI ($r_v = 0.66$) and persistence and MLI ($r_p = 0.58$). Roughly three times more cells had mitochondria localized anterior versus posterior in MDA-MB231, PC3, PC3M (PC3 cells selected for their metastatic abilities), and MDA-MB435 cell lines (Fig. 3 *C*).

The correlations between MLI, speed, and persistence were present in channels having a larger width (10 and 25 μm). In larger channels, MDA-MB-231 cells migrated with similar average velocity as in narrower channels, but were significantly less persistent ($r_p = 0.29$) (Fig. 3 *D*). Interestingly, the fraction of anterior-localized cells decreased with increasing channel width. Although both 10×6 and 25×6 μm cross-section channels guide predominantly anterior-localized cells, there was a decreasing trend of anterior localization with increasing cross section (Fig. 3 *E*). Movie S2 and Movie S3 show MDA-MB-231 cells moving more slowly and less persistently in channels of a wider cross section.

Effects of variegated mechanical confinements

To distinguish between passive and active mechanisms of anterior mitochondria localization during cell migration,

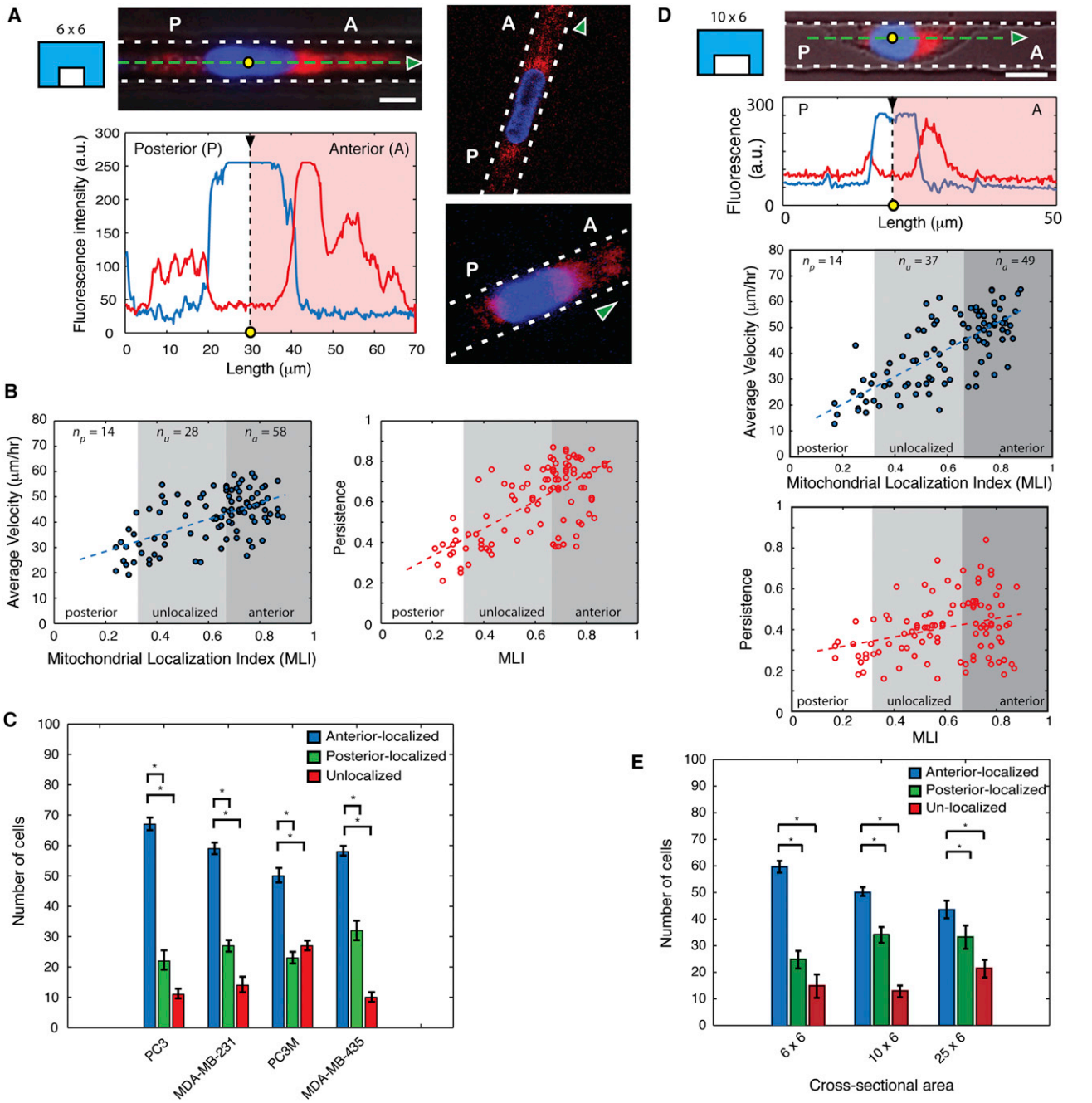

FIGURE 3 Mitochondrial localization during the migration of the epithelial cancer cell in constrained environments. (*A*) Representative fluorescence image showing breast cancer cell migrating through a 6 × 6 μm cross-section channel with anterior-localized mitochondria. Anterior and posterior regions are denoted as A and P. Dashed green line indicates region of fluorescence line scan, yellow dot indicates centroid, green arrowhead direction of migration, and dashed white lines the sidewalls of the channel. Scale bar 8 μm. Right panels show representative confocal images showing three-dimensional organization of mitochondria. Similarly, arrowheads indicate direction of migration and dashed white lines the sidewalls of channels. (*B*) Correlation of 100 single cells migrating in 6 × 6 μm cross-section channels indicate distinct relationships between MLI and migration velocity (*blue circles*, $r_v = 0.66$), and between MLI and persistence (*red circles*, $r_p = 0.58$). Least-squares fits for velocity (m = 0.4, $R^2 = 0.43$) and persistence (m = 0.66, $R^2 = 0.34$) are indicated by blue and red dashed lines, respectively. (*C*) Binning of localizations across 4 epithelial cell types with a predominant number of cells anterior-localized (PC3, PC3M, MDA-MB-231, and MDA-MB-435), * symbols designate statistically significant differences ($p < 0.05$). (*D*) Representative image of anterior localized cells in 6 × 10 μm cross-section channel, yellow dot indicates centroid and green arrowhead the direction of migration. Dashed white lines indicate the sidewalls of the channel. Scale bar 10 μm. Line scans of fluorescence (taken along *green dashed*) show anterior localization of mitochondria. Scatter plots (*lower panels*) suggest stronger correlations between MLI and average velocity (*blue circles*, $r_v = 0.74$) and weaker correlations between MLI and persistence (*red circles*, $r_p = 0.29$). Least-squares fits for velocity (m = 0.66, $R^2 = 0.55$) and persistence (m = 0.23, $R^2 = 0.08$) are indicated by blue and red dashed lines, respectively. (*E*) Bar plots showing decreasing number of anterior-localized cells with increasing channel cross-sectional area (ranging from 6 × 6 to 25 × 6 μm cross-section channels). Similarly, * symbols designate statistically significant differences ($p < 0.05$).

we observed the relocalization of mitochondria in cells moving through channels of alternating wide and narrow channels. In these experiments, we took advantage of the observation that MLI is sensitive to the increase in width of the channels. The fraction of cells with anterior-localized mitochondria decreased as the channel cross section increases from 36 to 150 μm^2. Dynamics of mitochondrial localization can be observed in wider channels (as shown in Fig. 4 *A* and Movie S4) with cells showing changes from anterior to posterior localization. As shown in Fig. 4 *B*, the decreased MLI in wider channels was promptly restored when cells entered the narrower sections. If passive mechanisms were responsible for mitochondrial relocalization, one would have expected progressive reduction in MLI during the advance through alternating wide and narrow channels. This observation suggests the presence of an active mechanism redistributing the mitochondria within migratory cells. Movie S5 and Movie S6 show anterior- and posterior-localized cells, respectively, traversing a narrow 6 × 6 μm cross-section constriction. Anterior-localized cells migrated efficiently through the small sections of the channels, whereas posterior-localized cells were severely delayed at the entrance to the constriction, suggestive for an active mechanism for mitochondrial localization. Importantly, the correlation between the ability to navigate constrictions efficiently and high MLI was conserved across epithelial cancer cell lines derived from prostate and breast lineages (PC3 and MDA-MB-435), as shown in Fig. 4 *C*.

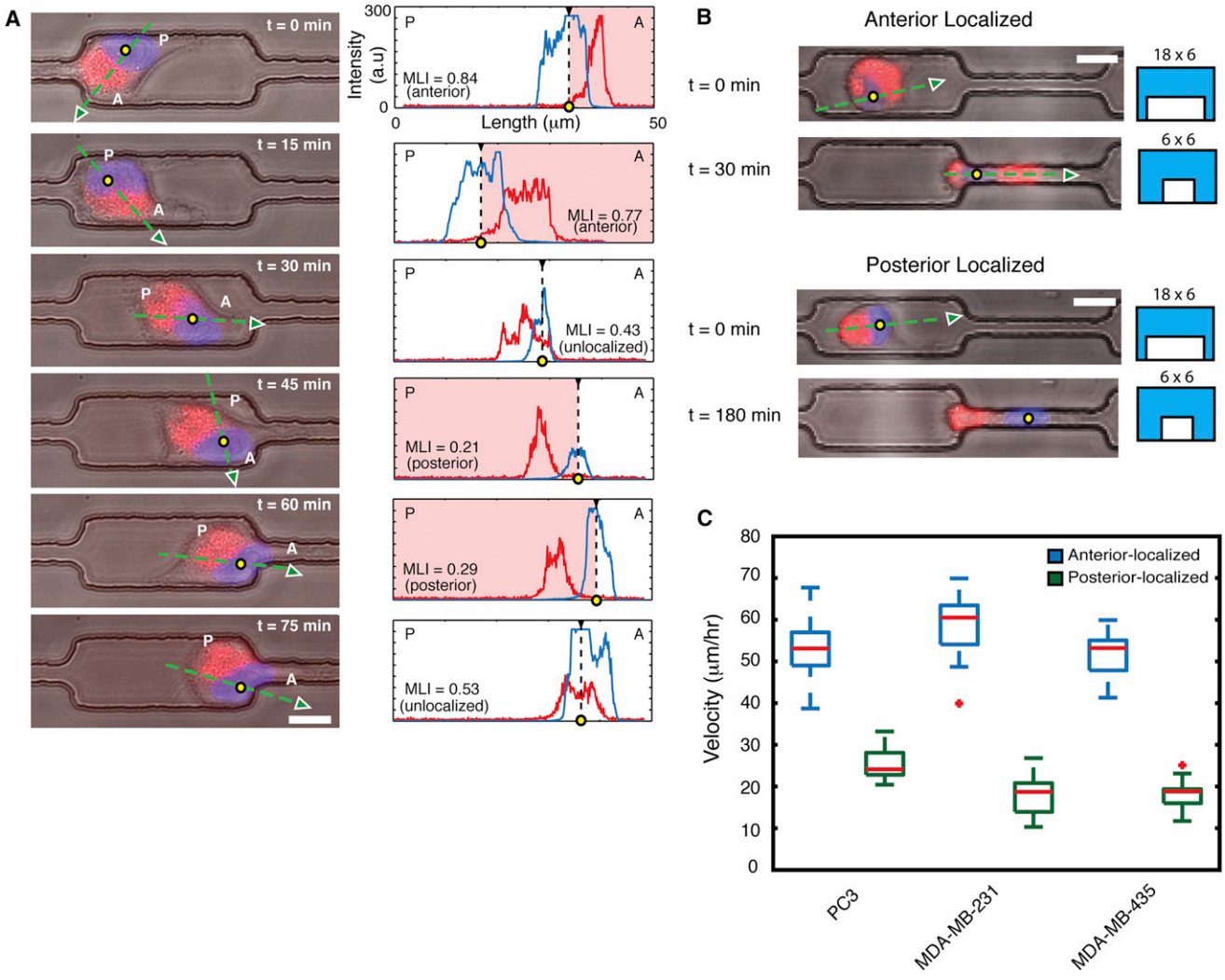

FIGURE 4 Mitochondrial relocalization during the migration of the cancer cell in variegated mechanical confinements. (*A*) Time series of a single breast cancer epithelial cell relocalizing mitochondria in a larger chamber. Dashed green line indicates region of fluorescence line scan, yellow dot indicates centroid, and green arrowhead direction of migration. Anterior and posterior regions of the cell are denoted as A and P. Localizations cycle through anterior, unlocalized to posterior, with the cell remaining stuck in the constriction and unable to continue migrating. Scale bar 10 μm. (*B*) Representative composite fluorescence and bright field images of anterior- and posterior-localized cells traversing channels of a varying cross section. Scale bar 12 μm. (*C*) Quantification of average cell velocity of three different epithelial cancer cell lineages (PC3, MDA-MB-231, and MDA-MB-435) cells with anterior- and posterior-localization traversing such variegated confinements.

Effects of mechanical confinements and biochemical gradients

In the presence of externally imposed EGF gradients (24), distinct mitochondrial localizations inside moving MDA-MB-231 cells were evident, as depicted in Fig. 5 *A*. Even though cells introduced in the channels had random orientations, during migrating in confinements with superimposed biochemical gradients they showed high correlations between both velocity and MLI ($r_v = 0.83$) and persistence and MLI ($r_p = 0.70$), as shown in Fig. 5 *B*. Plots of average velocity versus persistence showed a distinct clustering of high velocity and high persistence cells (Fig. 5 *C*), with higher correlations for anterior-localized cells with velocity and persistence ($r_{anterior} = 0.45$), compared to unlocalized ($r_{unlocalized} = 0.20$) and posterior-localized ($r_{posterior} = 0.15$) cells. Importantly, these highly migratory phenotypes were comprised almost entirely of anterior-localized cells (*red circles*). As seen in our results from migration platforms across various microenvironments anterior localization of mitochondria was closely coupled to both migration velocity and persistence. High persistence and high velocity were characteristics of anterior-localized cells (as seen in Fig. 5 *C*) and are indicative of a new and important migratory phenotype of epithelial cancer cells.

Effects of mitochondrial fission-fusion perturbations on migration

To probe the cause-effect relationship between mitochondrial localization and cell migration, we employed four cell lines in which mitochondrial fission (drp-1) or fusion (opa-1) proteins are manipulated by generating dominant-negative mutations or by promoting wild-type (WT) protein overexpression. These manipulations interfere with the dynamics of mitochondrial networks and the ability of individual mitochondrial to dynamically relocate within cells (26). Dominant-negative mutations of drp-1 (denoted as $DRP1^{K38A}$) yielded structurally larger mitochondria by inhibiting the mitochondrial network fragmentation. Overexpression of WT opa-1 (denoted as $OPA1^{overexp}$) also resulted in larger mitochondria, by stimulating the fusion of mitochondria (Fig. 6 A, *left panel*). Super-resolution microscopy images of fission-defective ($DRP1^{K38A}$) and fusion overexpressing ($OPA1^{overexp}$) mutants confirmed the presence of larger mitochondrial morphology as compared to WT cells (Fig. 6 *A*, *right panel*). As expected, these larger mitochondria were less efficiently transported and their distribution in migrating cells will be more homogenous than in the WT cells. In moving $DRP1^{K38A}$ cells, mitochondria were most often uniformly distributed within cells, and we could rarely observe any cells with front localization of mitochondria (Fig. 6 *B*). Conversely, smaller size mitochondria in overexpressing WT drp-1 (denoted as $DRP1^{overexp}$) and dominant-negative forms of opa-1 (denoted as $OPA1^{K301A}$), appeared to be effectively transported within cells, and their distribution was comparable to those in WT cells.

We found significant decreases in migration velocity and persistence in the mutant cells with larger mitochondria fission-defective ($DRP1^{K38A}$; Movie S7) and fusion overexpressing ($OPA1^{overexp}$) mutants compared with WT cells. For $DRP1^{K38A}$ cells the correlations between velocity, persistence, and MLI ($r_v = 0.24$ and $r_p = 0.11$) were significantly lower than in WT cells ($r_v = 0.78$ and $r_p = 0.82$) migrating under the exact same conditions. Comparably, for $OPA1^{overexp}$ correlations between velocity, persistence, and MLI ($r_v = -0.08$ and $r_p = 0.24$) were significantly lower than in WT cells. Conversely, in cells with mutations that resulted in mitochondria with a smaller size, mitochondrial redistribution within moving cells was comparable to that in WT cells ($DRP1^{overexp}$ and $OPA1^{K301A}$), and the speed and persistence were comparable to WT cells (Fig. S4). To further underscore this point, Movie S8 and Movie S9 show representative anterior-localized $DRP1^{overexp}$ cells and $OPA1^{K301A}$ cells, respectively, persistently traversing 6×6 μm cross-section channels. Moreover, scatter plots of migration characteristics versus MLI for $DRP1^{overexp}$ cells and $OPA1^{K301A}$ cells are comparable to those of WT cells (Fig. S4). To verify that any differences in cell migration were not due to energy production, we measured ATP production in all four mutants and found no significant defects (Fig. 6 *E*).

Interestingly, we noticed a progressive impairment of migration speed and persistence in the small numbers of anterior-localized $DRP1^{K38A}$ cells and anterior-localized $OPA1^{overexp}$ cells moving through channels with 6×6 μm cross-section channels (Movie S10 and Movie S11, respectively). Although the $DRP1^{K38A}$ and $OPA1^{overexp}$ cells had larger mitochondria that were not efficiently repositioned inside the migrating cells, these results suggested that mitochondrial redistribution inside the moving cells could be an important contributing factor to efficient migration. Furthermore, fission-defective $DRP1^{K38A}$ cells were observed in channels of variegated dimensions, migrating with a low velocity, unable to relocalize a mitochondrial network, and unable to effectively traverse a narrow, 6×6 μm cross section, constrictions (Movie S12). Together, these results indicate that, in addition to mitochondrial localization, mitochondrial redistribution inside moving cells is critical for the efficient migration through channels.

Effects of mitochondrial-microtubule linkage perturbations

Mitochondrial rhoGTPases, such as miro-1 and miro-2 play an important role in distributing mitochondria along microtubule networks (*schematically depicted* in Fig. 7 *A*) and as such play a role in shaping the mitochondrial network (27,28). Small hairpin RNA mediating knockdowns for

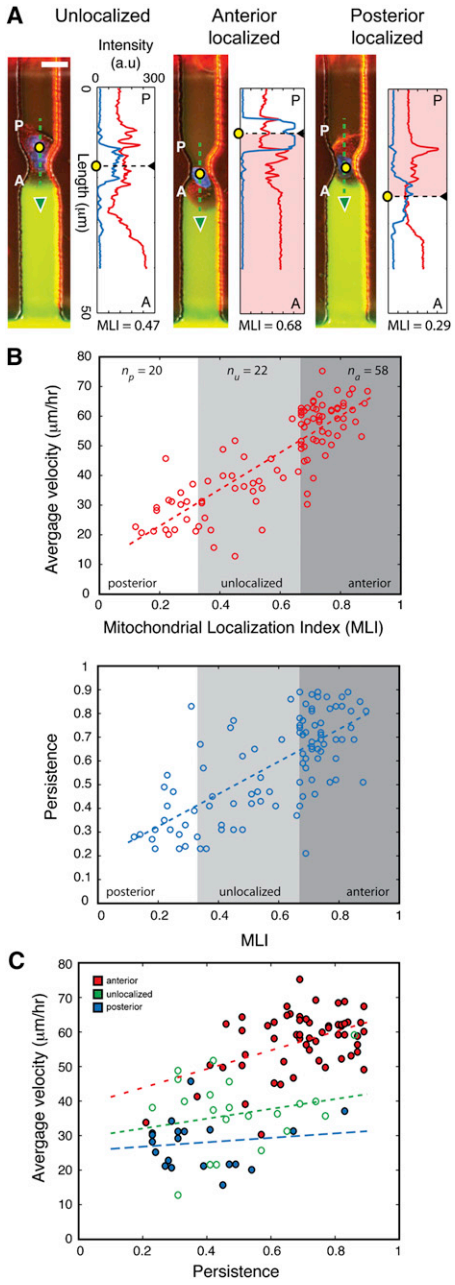

FIGURE 5 Mitochondrial localization with superimposed mechanical and chemical cues. (*A*) Representative images of anterior-, posterior-, and unlocalized cells migrating in channels with superimposed biochemical gradients of EGF (*green fluorescence*). Yellow dots indicate centroids of cells and green arrowheads direction of migration. Anterior and posterior regions are denoted as A and P. Corresponding line scans (*green dashed line*) show traces of mitochondrial (*red*) and nuclear (*blue*) fluorescence intensities. Scale bar 20 μm. (*B*) Cells migrating in response to growth factor gradients show strong relationships between migration velocity and MLI ($r_v = 0.83$) and also with MLI and persistence ($r_p = 0.70$). Linear least-squares fits for velocity (m = 0.77, $R^2 = 0.69$) and persistence (m = 0.68, $R^2 = 0.49$) are indicated by red and blue dashed lines, respectively. (*C*) Correlation between velocity and persistence shows a distinct clustering of high velocity and high persistent cells, which are anterior-localized (*red circles*) as compared to posterior-localized (*blue circles*), and unlocalized (*green circles*) cells that have low velocity and low persistence. Least-squares fits for anterior-localized (m = 0.34, $R^2 = 0.21$), unlocalized (m = 0.17, $R^2 = 0.04$), and posterior-localized (m = 0.08, $R^2 = 0.02$) cells are indicated by *red*, *green*, and *blue dashed lines*, respectively.

miro-1 have been previously shown to have a marked ability to disrupt mitochondrial transport (29). Analogously, we employed RNA interference techniques to selectively knockdown miro-1 and verified that disruption of miro-1 expression would disrupt mitochondrial localization without perturbing tubulin (Fig. 7 *A*, *lower left panel*). Importantly, knockdown of miro-1 did not significantly perturb mitochondrial function with ATP levels between miro-1 knockdowns and WT cells being comparable (Fig. 7 *A*, *lower right panel*). Furthermore, super-resolution imaging elucidated the decoupling between the mitochondrial network and the microtubule network in knockdowns of miro-1 (Fig. 7 *B*). Knockdowns of miro-1 displayed mitochondria that were predominantly unlocalized within moving cells, as shown in Fig. 7 *C*. Movie S13 shows a cell with unlocalized mitochondria migrating slowly and with low persistence through a 6 × 6 μm cross-section channel. Importantly, for migrating miro-1 knockdown cells correlations between velocity, persistence, and MLI ($r_v = -0.07$ and $r_p = 0.30$) were significantly lower than in WT cells ($r_v = 0.78$ and $r_p = 0.82$) migrating under the exact same conditions (as shown in Fig. 7 *D*).

DISCUSSION

We found that a strong correlation exists between the preferential front localization of mitochondria in motile cells and velocity and persistence during directional migration. We show that mitochondrial localization occurs in moving epithelial cancer cells and that anterior localization of mitochondria is necessary for faster and more persistent migration. Cells with anterior-localized mitochondria can navigate mechanical constraints and traverse narrowing channels approximately three times faster and are approximately three times more persistent in the same direction than cells not displaying such a phenotype. Moreover, we show that perturbing the redistribution of mitochondria within cells by mutations in the mitochondrial fusion and fission proteins reduces the number of cells with anterior-localized mitochondria and renders the cells unable to migrate with high speed and directional persistence in mechanically confined environments. Similarly, interfering with the expression of the mitochondrial rhoGTPase-1 (miro-1), which links mitochondria to microtubules and aids in their transport, also reduces the migratory abilities of cancer cells. These effects are observed for both speed and persistence of migration, underscoring the importance of mitochondrial intracellular localization during the fast and persistent migration of epithelial cancer cells.

Our observations of preferential anterior localization of mitochondria in the fastest and most persistent epithelial

cancer cells are different from those previously reported in lymphocytes. In lymphocytes, mitochondria are most often localized between the nucleus and the trailing edge (i.e., posterior localization) during chemokine-induced migration (6). The differences in mitochondrial localization between epithelial and myeloid cells are not entirely surprising. Other organelles also have distinct localizations in the two cell types during migration. For example, the location of the microtubule organizing center has been shown to be preferentially ahead of the nucleus in motile epithelial cells (2) and behind the nucleus in motile lymphocytes (30,31). Additionally, the location of the endoplasmic reticulum and the Golgi apparatus is predominantly behind the nucleus in moving epithelial cells (4) and in front of the nucleus in macrophages during chemotaxis (32). Interestingly, our observations are different from the preliminary results reported in the study for epithelial cells (6). Unlike the micropipette assays used previously (6), in our study we relied on microfluidic assays, which are better suited for more precise measurements, provide higher throughput, and enable observations over longer time durations. These differences in methods are particularly important because mitochondrial repositioning to the front of epithelial cells requires several hours after the start of directional migration. Taken together, to our knowledge, our specifically engineered platforms have enabled observations of new roles of mitochondrial networks in migrating epithelial cancer cells, pointing to a role of these dynamic networks in facilitating cancer cell migration.

Cellular motility is a complex phenotype that can be deconstructed and characterized precisely using measures of velocity and directional persistence. Typically, the movement of cells on flat surfaces is recorded by time-lapse imaging over extended periods and the trajectory of the cells is tracked and analyzed using sophisticated methods. In this study, we took advantage of microfluidic tools that restrict the migration of cells to one-dimensional channels and enable quick and precise characterization of cancer cell motility speed and directionality (20,21). By superimposing mitochondrial localization (quantified as MLI) on these traditional measures of migration, we identified migratory phenotypes directly related to the mitochondrial distribution within motile cells. Interestingly, in the presence of guiding gradients or mechanical confinement, cells with mitochondria localized in an anterior position consistently display faster migration and higher persistence. The location of mitochondria within cells also enabled us to cluster the cells that are both the fastest moving and most persistent. This observation is important if one assumes that the overall capacity of a cell to invade is proportional to the multiplicative effect of speed and persistence. With this assumption, cells that move three times faster and are three times more persistent than the ensemble average, could invade one order of magnitude further than the average cells. At the timescale of cancer cell invasion, this could mean differences from months to years for cancer cells to invade over longer distances, e.g., to reach distant lymph nodes by migration through lymphatics. Importantly, high persistence and high velocity are unique characteristics of anterior localization of mitochondria in migrating epithelial cancer cells and as such are indicative of an important migratory phenotype. Our work shows the ability to identify such migratory phenotypes in otherwise homogenous cell populations. It also points to the possibility that mitochondrial localization could be used as a marker to identify cancer cells that possess more aggressive invasive capabilities.

Further studies are necessary to identify the precise stimuli that direct the redistribution of mitochondria within moving epithelial cells. At least two hypotheses are emerging from existing studies. First, higher bioenergetic demands at the leading edge of active actin polymerization could require higher mitochondrial density. Such guidance of mitochondria has been previously reported in axons and dendrites, correlated closely with the high energy demand needed to generate action potentials in these structures (9,10). The differences in mitochondrial localization between lymphocytes and epithelial cancer cells could also be attributed to underlying differences in modes of migration—with uropods in lymphocytic cells pushing the cell forward and conversely pseudopods in epithelial cells pulling the cell forward. Second, calcium signaling could also play an important role. This role is suggested by the differences in mitochondrial localization between lymphocytes and epithelial cells observed in this study, and by the underlying differences in their intracellular calcium distribution dynamics. In lymphocytic cells, during chemokine-induced migration, mitochondria accumulate to the posterior of cells (6), correlated with higher calcium levels (30). In epithelial cells, more calcium is being allowed to enter the cells at the anterior end (33). Separately, increased intracellular calcium concentrations have been shown to modulate mitochondrial motility and to sequester mitochondria in regions of high intracellular Ca^{2+} (34). It is possible that by quickly buffering the Ca^{2+} that enters the cells (35), mitochondria regulate the Ca^{2+} levels at the front of the moving cells, maintain the sensitivity to new stimuli, and overall contribute to persistent migration. Both hypotheses remain to be tested in further studies.

In conclusion, our results show that the redistribution of mitochondria to the anterior of moving cancer cells is a necessary condition for faster and more persistent migration. Considering the correlations between the speed and persistence of cells migrating through channels and the rate of metastasis formation in an animal model demonstrated in previous studies (36), our results could lead to new approaches to identifying the specific subpopulation of tumor cells with propensity to metastasize faster and over longer distances. In the future, studies of organelle reorganization could facilitate a better understanding of the mechanisms of cancer cell migration and could help

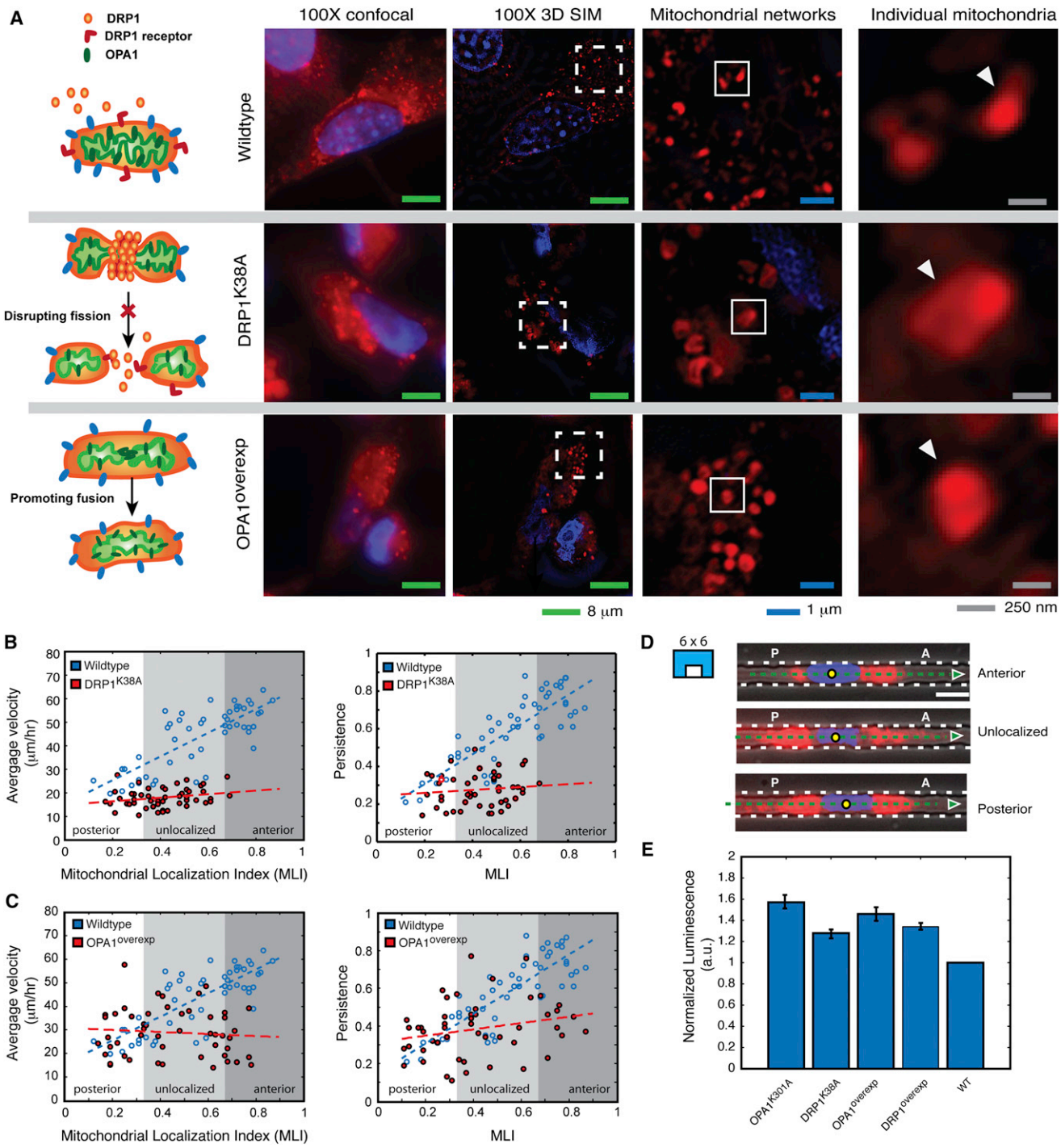

FIGURE 6 Interfering with mitochondrial shape dynamics alter mitochondrial localization and the migration of cancer cells in constrained environments. (*A*) Schematic depicting role of drp-1 and opa-1 proteins in mitochondrial shape dynamics. Drp-1 dimerizes and forms constructs that are responsible in breaking mitochondria apart and thereby enabling the cell to redistribute mitochondria and better meet energy requirements during events of high bioenergetic need. Conversely, opa-1 fuses the inner membranes of the mitochondria and serves as a binding protein to fuse distinct mitochondria into larger entities. Super-resolution images of representative WT and mutant cells show that drp-1 mutants and opa-1 overexpression result in significantly larger mitochondria than WT cells. Both images of mitochondrial networks (*middle panels*) and individual mitochondria (*right panels*, highlighted with *white arrowheads*) show evidence of this. (*B*) Breakdown in correlation between the velocity of migration and MLI can be calculated in $DRP1^{K38A}$ mutants (*red circles*, $r_v = 0.24$ compared to WT cells (*blue circles*, $r_v = 0.78$). Similarly, a breakdown in correlation between the persistence of migration and MLI can be calculated in $DRP1^{K38A}$ mutants (*red circles*, $r_p = 0.11$) compared to WT cells (*blue circles*, $r_p = 0.82$), suggesting a strong role for anterior localization of mitochondria in epithelial cancer cell migration. Least-squares fits for mutants show near independence of migration velocity (*dashed red line*, m = 0.09, $R^2 = 0.06$) and persistence (*dashed red line*, m = 0.07, $R^2 = 0.01$) with MLI, compared to WT cells that display strong correlations of velocity (*dashed blue line*, m = 0.63, $R^2 = 0.61$) and persistence (*dashed blue line*, m = 0.79, $R^2 = 0.68$) with MLI. (*C*) Analysis of the average velocity, persistence for $OPA1^{overexp}$ mutants

(legend continued on next page)

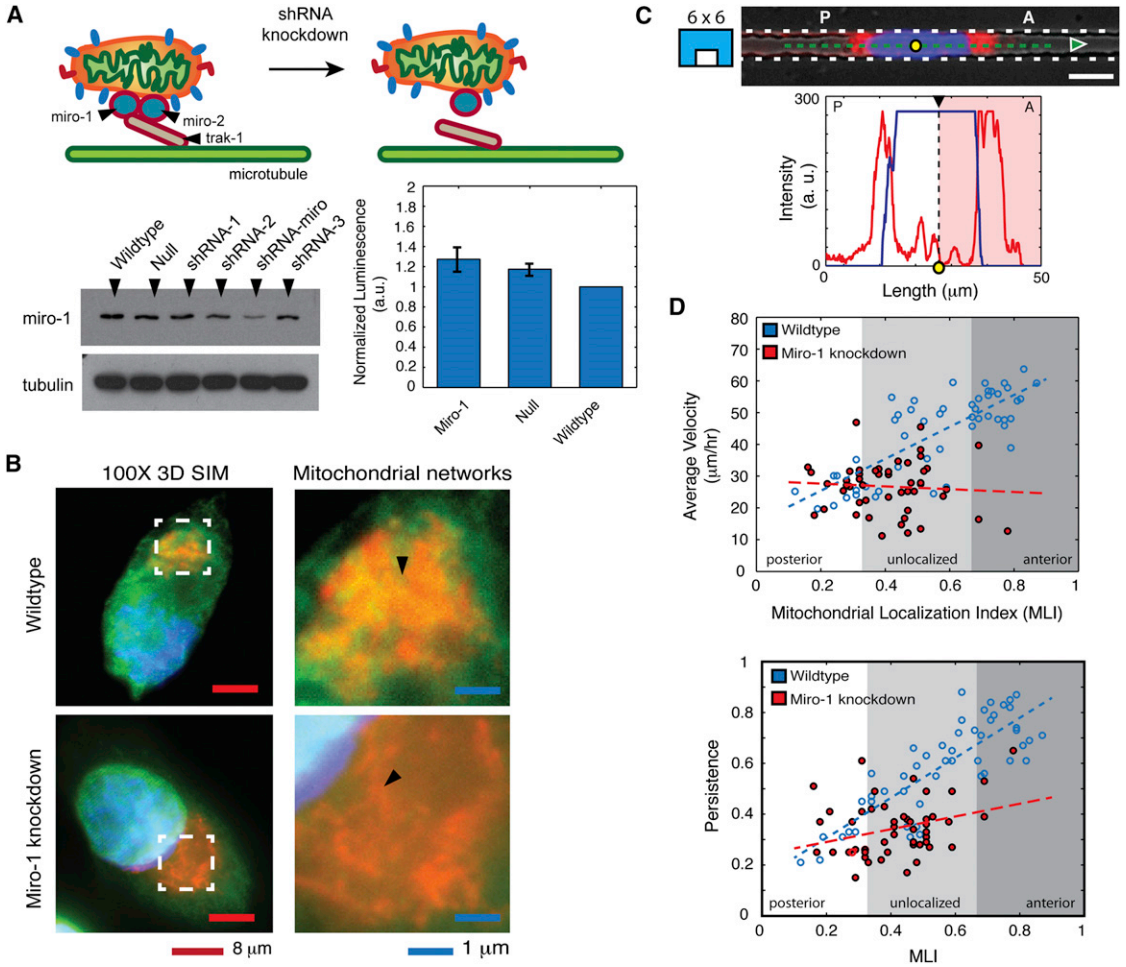

FIGURE 7 Interfering with mitochondria-microtubule linkage alters mitochondrial localization and the migration of cancer cells in constrained environments. (*A*) Top panel shows schematic of mitochondria attached to microtubules through mitochondrial rhoGTPases such as miro-1 and miro-2. Western blot analysis of knockdowns shows that a specific hairpin significantly alters miro-1 production without altering microtubule expression (as shown in *tubulin blot*). Additionally, knockdowns are also bioenergetically similar to WT cells in terms of ATP levels (*right panel*). (*B*) Super-resolution microscopy images show a loss of colocalization between mitochondria and microtubules in miro-1 knockdowns (highlighted by *black arrowheads*), whereas they are highly colocalized in WT cells. (*C*) Miro-1 knockdowns in breast cancer epithelial cells migrating through a 6 × 6 μm cross-section channel show a loss of mitochondrial localization. Yellow dot indicates the cell centroid, green arrowhead the direction of migration, and dashed green line the line trace for the fluorescence scan (*lower panel*). Anterior and posterior regions are denoted as A and P. Scale bar 10 μm. (*D*) Scatter plots of average velocity (*left panel*, *red circles*, $r_v = -0.07$) and persistence (*right panel*, *red circles*, $r_p = 0.30$), show a distinct breakdown in correlation between MLI and velocity and persistence in miro-1 knockdowns compared to WT cells (*blue circles*, $r_v = 0.78$ and $r_p = 0.82$). Least-squares fits for miro-1 knockdowns show near independence of migration velocity (*left panel*, *dashed red line*, m = −0.05, $R^2 = 0.01$) and persistence (*right panel*, *dashed red line*, m = 0.25, $R^2 = 0.09$).

uncover new biomarkers for the metastatic capabilities of tumorigenic cells.

SUPPORTING MATERIAL

Supporting methods, figures, and movies are available at http://www.biophysj.org/biophysj/supplemental/S0006-3495(13)00335-4.

We thank Thomas Diefenbach for assistance with confocal microscopy, which was performed at the Ragon Institute Microscopy Facility of Massachusetts General Hospital. We thank Eliza Vasile for assistance with super-resolution microscopy, which was performed at the Imaging Core Facility, Koch Institute of Integrative Cancer Research at the Massachusetts Institute of Technology.

This work was supported by the ECOR MGH-MIT Fellowship in Translational Medicine and National Institutes of Health grants

migrating through 6 × 6 μm cross-section channels also reveals independence between velocity, persistence, and MLI. Least-squares fits for mutants show near independence of migration velocity (*dashed red line*, m=0.05, $R^2 = 0.01$) and persistence (*dashed red line*, m = 0.17, $R^2 = 0.05$). Plots and least-squares fits for WT cells (*blue circles* and *dashed lines*, respectively) are identical to those in (*B*). (*D*) Representative fluorescence images showing $DRP1^{K38A}$ breast cancer cells migrating through 6 × 6 μm cross-section channels showing canonical localizations of mitochondria. Arrowheads indicate the direction of migration and yellow dots the cell centroid. Anterior and posterior regions are denoted as A and P. Scale bar 8 μm. (*E*) ATP assays show that both mutant and WT cells are bioenergetically similar.

CA135601, GM092840, and EB002503. S.N.B. is a Howard Hughes Investigator.

REFERENCES

1. Ridley, A. J., M. A. Schwartz, …, A. R. Horwitz. 2003. Cell migration: integrating signals from front to back. *Science.* 302:1704–1709.
2. Yvon, A. M., J. W. Walker, …, P. Wadsworth. 2002. Centrosome reorientation in wound-edge cells is cell type specific. *Mol. Biol. Cell.* 13:1871–1880.
3. Miller, P. M., A. W. Folkmann, …, I. Kaverina. 2009. Golgi-derived CLASP-dependent microtubules control Golgi organization and polarized trafficking in motile cells. *Nat. Cell Biol.* 11:1069–1080.
4. Pouthas, F., P. Girard, …, E. G. Reynaud. 2008. In migrating cells, the Golgi complex and the position of the centrosome depend on geometrical constraints of the substratum. *J. Cell Sci.* 121:2406–2414.
5. Uetrecht, A. C., and J. E. Bear. 2009. Golgi polarity does not correlate with speed or persistence of freely migrating fibroblasts. *Eur. J. Cell Biol.* 88:711–717.
6. Campello, S., R. A. Lacalle, …, A. Viola. 2006. Orchestration of lymphocyte chemotaxis by mitochondrial dynamics. *J. Exp. Med.* 203:2879–2886.
7. Lewis, M. R., and W. H. Lewis. 1914. Mitochondria in tissue culture. *Science.* 39:330–333.
8. Hollenbeck, P. J., and W. M. Saxton. 2005. The axonal transport of mitochondria. *J. Cell Sci.* 118:5411–5419.
9. Morris, R. L., and P. J. Hollenbeck. 1995. Axonal transport of mitochondria along microtubules and F-actin in living vertebrate neurons. *J. Cell Biol.* 131:1315–1326.
10. Frederick, R. L., and J. M. Shaw. 2007. Moving mitochondria: establishing distribution of an essential organelle. *Traffic.* 8:1668–1675.
11. Brown, E. B., R. B. Campbell, …, R. K. Jain. 2001. In vivo measurement of gene expression, angiogenesis and physiological function in tumors using multiphoton laser scanning microscopy. *Nat. Med.* 7:864–868.
12. Condeelis, J., and J. E. Segall. 2003. Intravital imaging of cell movement in tumours. *Nat. Rev. Cancer.* 3:921–930.
13. Farina, K. L., J. B. Wyckoff, …, J. G. Jones. 1998. Cell motility of tumor cells visualized in living intact primary tumors using green fluorescent protein. *Cancer Res.* 58:2528–2532.
14. Hazan, R. B., G. R. Phillips, …, S. A. Aaronson. 2000. Exogenous expression of N-cadherin in breast cancer cells induces cell migration, invasion, and metastasis. *J. Cell Biol.* 148:779–790.
15. Ma, L., J. Teruya-Feldstein, and R. A. Weinberg. 2007. Tumour invasion and metastasis initiated by microRNA-10b in breast cancer. *Nature.* 449:682–688.
16. Zeng, Q., J. M. Dong, …, W. Hong. 2003. PRL-3 and PRL-1 promote cell migration, invasion, and metastasis. *Cancer Res.* 63:2716–2722.
17. Hanahan, D., and R. A. Weinberg. 2011. Hallmarks of cancer: the next generation. *Cell.* 144:646–674.
18. Calbo, J., E. van Montfort, …, A. Berns. 2011. A functional role for tumor cell heterogeneity in a mouse model of small cell lung cancer. *Cancer Cell.* 19:244–256.
19. Heppner, G. H. 1984. Tumor heterogeneity. *Cancer Res.* 44:2259–2265.
20. Irimia, D., and M. Toner. 2009. Spontaneous migration of cancer cells under conditions of mechanical confinement. *Integr. Biol. (Camb).* 1:506–512.
21. Scherber, C., A. J. Aranyosi, …, D. Irimia. 2012. Epithelial cell guidance by self-generated EGF gradients. *Integr. Biol. (Camb).* 4:259–269.
22. Pankov, R., Y. Endo, …, K. M. Yamada. 2005. A Rac switch regulates random versus directionally persistent cell migration. *J. Cell Biol.* 170:793–802.
23. Irimia, D., G. Charras, …, M. Toner. 2007. Polar stimulation and constrained cell migration in microfluidic channels. *Lab Chip.* 7:1783–1790.
24. Ambravaneswaran, V., I. Y. Wong, …, D. Irimia. 2010. Directional decisions during neutrophil chemotaxis inside bifurcating channels. *Integr. Biol. (Camb).* 2:639–647.
25. Jones, C. N., J. Dalli, …, D. Irimia. 2012. Microfluidic chambers for monitoring leukocyte trafficking and humanized nano-proresolving medicines interactions. *Proc. Natl. Acad. Sci. USA.* 109:20560–20565.
26. MacAskill, A. F., and J. T. Kittler. 2010. Control of mitochondrial transport and localization in neurons. *Trends Cell Biol.* 20:102–112.
27. Fransson, A., A. Ruusala, and P. Aspenström. 2003. Atypical Rho GTPases have roles in mitochondrial homeostasis and apoptosis. *J. Biol. Chem.* 278:6495–6502.
28. Fransson, S., A. Ruusala, and P. Aspenström. 2006. The atypical Rho GTPases Miro-1 and Miro-2 have essential roles in mitochondrial trafficking. *Biochem. Biophys. Res. Commun.* 344:500–510.
29. Macaskill, A. F., J. E. Rinholm, …, J. T. Kittler. 2009. Miro1 is a calcium sensor for glutamate receptor-dependent localization of mitochondria at synapses. *Neuron.* 61:541–555.
30. del Pozo, M. A., M. Nieto, …, F. Sánchez-Madrid. 1998. The two poles of the lymphocyte: specialized cell compartments for migration and recruitment. *Cell Adhes. Commun.* 6:125–133.
31. Luxton, G. W., and G. G. Gundersen. 2011. Orientation and function of the nuclear-centrosomal axis during cell migration. *Curr. Opin. Cell Biol.* 23:579–588.
32. Nemere, I., A. Kupfer, and S. J. Singer. 1985. Reorientation of the Golgi apparatus and the microtubule-organizing center inside macrophages subjected to a chemotactic gradient. *Cell Motil.* 5:17–29.
33. Evans, J. H., and J. J. Falke. 2007. Ca2+ influx is an essential component of the positive-feedback loop that maintains leading-edge structure and activity in macrophages. *Proc. Natl. Acad. Sci. USA.* 104:16176–16181.
34. Yi, M., D. Weaver, and G. Hajnóczky. 2004. Control of mitochondrial motility and distribution by the calcium signal: a homeostatic circuit. *J. Cell Biol.* 167:661–672.
35. Bick, A. G., S. E. Calvo, and V. K. Mootha. 2012. Evolutionary diversity of the mitochondrial calcium uniporter. *Science.* 336:886.
36. Wolfer, A., B. S. Wittner, …, S. Ramaswamy. 2010. MYC regulation of a "poor-prognosis" metastatic cancer cell state. *Proc. Natl. Acad. Sci. USA.* 107:3698–3703.

Mitochondrial Localization and the Persistent Migration of Epithelial Cancer cells

Salil P. Desai,[†‡] Sangeeta N. Bhatia,[†§] Mehmet Toner,[†‡] and Daniel Irimia[‡*]

[†]Harvard-MIT Division of Health-Science Technology, Massachusetts Institute of Technology, Cambridge, Massachusetts; [‡]Department of Surgery, Massachusetts General Hospital, Harvard Medical School, Boston, Massachusetts; and [§]Howard Hughes Medical Institute, Chevy Chase, Maryland.

Submitted May 22, 2012, and accepted for publication March 7, 2013.

*Correspondence: dirimia@hms.harvard.edu

SUPPLEMENTARY INFORMATION SECTION

Cell culture. MDA-MB-231, MDA-MB-435 and PC3 cell lines were obtained from the ATCC. The PC3M cell line was provided courtesy of the Lindquist Lab. MDA-MB-231 and MDA-MB435 cells were cultured in DMEM (with L-glutamine) supplemented with 10 % (v/v) fetal bovine serum, and 2% (v/v) penicillin-streptomycin. Cells were split and re-seeded at 1:10 split ratios every 2-3 days. PC3 and PC3M cells were cultured in 44% (v/v) F12K media, 44% (v/v) RPMI 1640 media, 10% (v/v) fetal bovine serum, and 2% (v/v) penicillin-streptomycin. Cells were split and re-seeded at 1:5 ratios every 3 days. For imaging and visualization, cells were labeled with nuclear-staining Hoechst (Invitrogen) and mitochondrial staining MitoTracker Red (Invitrogen) dyes. Briefly, prior to the experiment, Hoechst and MitoTracker Red (100 nM) were added to the culture media and cells were incubated with the dye cocktail for 1 hour. Cells were then removed from the incubator and washed twice with 1× phosphate-buffered saline (PBS). Cells were then detached from the surface using Accumax (Sigma) for 10 min at 37 °C, quenched with serum-containing culture media and centrifuged at 1500 rpm for 5 minutes. The cells were then re-suspended in ~100 µl of culture media (to yield a working concentration of ~10,000 cells/µl) and were loaded in the migration platform of interest.

Mutagenesis. Mutant versions of mitochondrial shaping proteins drp-1 and opa-1 were generated using standard site-directed mutagenesis techniques. The mutagenesis is pictorially depicted in Supplementary Figure S1. Briefly, plasmid pDONR223 backbones containing the human isoforms of drp1 and opa-1 were obtained from the Human ORFeome Collection (Center for Cancer Systems Biology, Dana-Farber Cancer Institute). Single amino acid, site-directed mutation primers were designed using Agilent's QuickChange primer design system and 35- to 40-mer primers were subsequently synthesized (Integrated DNA Technologies). Dominant-negative mutants of drp-1 (K38A) were generated using the Quickchange II kit (Agilent Technologies) and the following primers - sense 5'-gaacgcagagcagcggagcgagctcagtgctagaaa-3', and anti-sense 5'-tttctagcactgagctcgctccgctgctctgcgttc-3'. Similarly, dominant-negative mutants of

opa-1 (K301A) were generated using the following primers, sense 5'-tggagatcagagtgctggagcgactagtgtgttggaaatg-3', and anti-sense 5'-catttccaacacactagtcgctccagcactctgatctcca-3' (reverse). Using these primers, single amino acid mutations were performed using standard protocols following the manufacturer's directions (Agilent Technologies). Plasmids were purified using standard plasmid purification techniques (Hi-Speed Plasmid Prep Kit, Qiagen, Inc.) and purity/concentration of plasmid constructs were determined spectrophotometrically (ND-1000, Thermo Fisher Scientific). Plasmids containing EGFP driven by a CMV promoter were provided courtesy Mikko Taipele. Cells were transfected using standard lipid-based reagents (Lipofectamine 2000, Invitrogen) and after 48 hours were assessed for fluorescence expression. Individual mutant cells were identified, sorted and cloned as detailed in the following section. A schematic summarizing the mutagenesis technique is shown in Supplementary Figure S1.

Flow cytometry and cell cloning. Cells constitutively expressing enhanced green fluorescence protein (EGFP) were sorted for positive expression (windowed for 80-90th percentile) using a sorting flow cytometer (FACSAria, BD Biosciences). Cells were sorted into 96-well plates to obtain a single-cell per well on average. Well plates were then incubated at 37 °C (and 5% CO_2) for 72 hours to assess clonal expansion. Wells that contained viable clones were placed under selection pressure of 500 µg/ml geneticin (G-418, Invitrogen). Viable clones that contained both EGFP and antibiotic selection genes were then observed for another 48-72 hours. Five clones were picked and further expanded for two cell passages and then subsequently frozen down in 70% (v/v) culture media, 20% (v/v) FBS and 10% (v/v) dimethyl sulfoxide and stored in liquid nitrogen for further use.

RNAi knockdowns and western blotting. Knockdowns of mitochondrial rhoGTPase (miro/rhot-1) were generated using lentiviral constructs provided by the RNAi Consortium (TRC). Viral stocks were transduced in MDA-MB-231 cells using spin infection in the presence of 8 µg/ml polybrene. Cells were subsequently selected in

puromycin and expanded for proteomic analysis. Western blotting was performed using standard protocols. Briefly, whole-cell protein extracts were prepared in cold lysis buffer consisting of 100 mM NaCl, 30 mM Tris-HCl , 1% NP-40, 30 mM sodium fluoride, 1 mM EDTA, 1 mM sodium vanadate, and complete protease inhibitor cocktail tablet (Roche Diagnostics). Lysates were incubated on ice for 30 min and supernatants were recovered by centrifugation at 14,000 rpm at 4°C for 10 min. Proteins were then separated on NuPAGE Novex gels (Invitrogen) and transferred to PROTRAN nitrocellulose membrane (Whatman). Membranes were then blocked in blocking buffer (BB - 100 mM Tris (v/v), 0.25% (v/v) Tween 20 and 4.5% (w/v) NaCl, with 3% (w/v) Carnation milk powder) for 1 hour and subsequently washed with 1× PBS containing 0.1% (v/v) Tween-20. Membranes were probed with target antibodies — anti-rhot1 (4356, AbCam) diluted 1:50 (v/v) in buffer and anti-tubulin (RB9421, Thermo Fisher Scientific) diluted 1:100 (v/v) for 1hr at room temperature. The secondary antibody was diluted to 1:10,000 (v/v) in BB and incubated for 1 hour at room temperature with the blotted membrane. To perform the detection, reagents for enhanced chemiluminescence were mixed 1:1 and incubated with the blot followed by photographic film transfer and development.

ATP assays. Cellular lysates from ~1×10^6 cells were collected for measurement of intracellular ATP content. ATP content was determined using a bioluminescence detection kit (ENLITEN, Promega) according to the manufacturer's instructions, and using a luminescent plate reader (Tecan). ATP assays were performed on dominant-negative fission-fusion mutant cells ($DRP1^{K38A}$ and $OPA1^{K301A}$), wildtype fission-fusion protein over-expressing cells ($DRP1^{overexp}$ and $OPA1^{overexp}$), miro-1 knockdown cells and wildtype MDA-MB-231 cells.

Image acquisition and analysis. Migrating cells were imaged using a Nikon TiE microscope operating in epifluorescence mode and equipped with an incubation chamber. Time-lapse images were acquired at multiple spatial locations and multiple wavelengths every 15 or 20 minutes, and analyzed using custom MATLAB scripts. All fluorescence

images were acquired with 12-bit resolution using a cooled-CCD camera (QImaging). Care was taken to ensure that all images were recorded with identical acquisition parameters (exposure time, camera gain/gamma control and microscope aperture settings). The persistence of migration was quantified by determining the ratio between the shortest, linear distance from the starting point of a time-lapse recording to the end point (T) and the total distance traversed by the cell (D). This is further elucidated in Figure 1A-C for random migration, the distance traveled between time-points is denoted as $d_{time\text{-}point}$ and the shortest distance traveled is denoted by the straight, dashed line joining the start and end points and denoted by T. Thus, D is defined as the sum of $d_{time\text{-}point}$. The cell whose trajectory is mapped in Figure 1C (right panel) has a persistence = 0.12, as it effectively circles back to its starting position – at times maintaining a steady trajectory and at times rapidly changing direction. Accordingly, persistence values close to 1 indicated a cell moving directionally between two points with minimal deviations and a persistence values closer to 0 indicated a cell moving along multiple trajectories before arriving at the end-point. Persistence was computed for periods of 1 to 2 hours and for the same set of time points over which mitochondrial localization index information was collected.

Nuclear position analysis. The mitochondrial localization index (MLI) is quantified in relation to the centroid of the nucleus (which is also used to track cell location). To assess mitochondrial localization within cells, mitochondria (red-channel) and the nucleus (blue-channel) were fluorescently labeled and analyzed in conjunction with phase images of the whole cell (brightfield-channel). The centroid of the nucleus was used to mark the center of the cell. Line-scans of fluorescence in the red-channel were integrated before and after this cell mid-point in areas bounded by the extent of the cell. Hence, MLIs are sensitive to the position of the nucleus within the cell. To ensure there is no systematic bias in quantifying mitochondrial localization 100 cells from each migration condition were analyzed to show the position of the nucleus relative to the cell extents (we define this as the normalized nuclear position). This is both pictorially depicted and quantified in Figure S2. The top panel shows a canonical image of a MDA-MB-231 breast cancer cell spontaneously migrating through a microchannel. As in the main

manuscript, green arrowheads depict the direction of migration. The cell extents (depicted by blue dashed lines) represent the absolute the anterior and posterior boundaries of the cell. The distance between these boundaries provides a metric of the length or overall "extent" of the cell (denoted as *E*). The distance between the centroid of the nucleus (denoted by *C*) and the midpoint of the cell extents (denoted by *M)* provides a metric of the location of the nucleus relative to the cell body. This difference ($C - M$) is in turn normalized to *E*, to enable comparisons migrating through different conditions. Hence, a positive normalized nuclear position denotes the nucleus as "leading" in front of the midpoint of the cell and a negative normalized position denotes the nucleus "lagging" behind the cell's midpoint. In Figure S2, *M* is at 33 μm, *C* at 30 μm, and E is 53 – 13 μm = 40 μm, and hence the normalized nuclear distance is –0.075, indicative of the nucleus is "lagging" behind the middle of the cell. This normalized nuclear position was computed for 100 cells from each condition of migration described in the main manuscript. Importantly, cells show only a small variation in nuclear position indicative of minimum bias in the measurements of mitochondrial localization in a moving cell.

To assess mitochondrial localization within cells, mitochondria and the nucleus were fluorescently labeled as described above. The centroid of the nucleus was used to mark the center of the cell. Line-scans of mitochondrial fluorescence were integrated before and after the center of the cell. A mitochondrial localization (MLI) index was calculated as the ratio between the integrated area of the fore and the extent of the fore and aft spatial regions.. MLI greater than 0.65 was scored as anterior-localized, less than 0.35 was scored as posterior-localized, and between 0.35 and 0.65 was scored as un-localized. The index was measured repeatedly in a sequence of 4 to 8 time steps. For confocal microscopy, migrating cells were fixed in 3.7% paraformaldehyde (Sigma-Aldrich) for 1 hour. Fixed cells were subsequently imaged on a LSM5 confocal laser scanning microscope (Zeiss).

Super-resolution image acquisition and analysis. Drp-1 mutants, opa-1 mutants, miro-1 knockdowns, and wildtype MDA-MB-231 cells were plated on cover-slips and stained for mitochondria, tubulin (only in the case of miro-1 knockdowns) and nuclei. Cells were

fixed in 3.7% paraformaldehyde for 15 minutes, washed 3× in PBS, and then mounted on standard microscope slides using Fluoromont G (Sigma Aldrich). Cells were then imaged on a structured illumination microscope (OMX, DeltaVision) using a 100× (0.9 NA) oil immersion objective using 594 nm, 488 nm and 405 nm laser illumination lines.

Device Microfabrication. All devices were fabricated using standard single- and multi-layer soft lithography techniques. Unconstrained chemotaxis micro-devices (UCMs) depicted in Figure 2 and spontaneous migration micro-devices (SMMs) shown in Figures 3, 4, 6 and 7, were fabricated using two layers of photoresist. Briefly, piranha cleaned, single-side polished silicon wafers were dehydrate-baked and plasma cleaned. The first layer of SU-8 (SU-8 10, Microchem Corporation) was spun-on, baked, exposed to define the channel features. Chemokine reservoir and cell loading region features were defined using a second layer of SU-8 (SU-8 50, Microchem Corporation). Both layers were then developed using negative-resist developer for 2-5 minutes to generate the final master mold. Constrained migration micro-devices (CMMs, from Figure 5) were fabricated using two master molds. Briefly, the first master mold is fabricated with three SU-8 layers of 7 μm, 10 μm and 35 μm thicknesses. This mold forms the "flow" (bottom) layer of the CMM. The corresponding "control" (top) layer master mold of the CMM is fabricated using a 50 μm thickness SU-8 layer. Elastomeric devices were then fabricated using standard soft lithography fabrication techniques using (poly)dimethylsiloxane (Sylgard 184, Dow Corning) mixed at a 10:1 (w/w) ratio and cured overnight at 70 °C. Access holes were punched in devices using biopsy punches (Ted Pella, Inc.). Individual devices were bonded to cover-slip bottom 24-well plates (MatTek Corporation) or single-well cover-slip bottom dishes (Willco Wells) after exposure to a 20-second, radio frequency generated plasma (March Corporation). In the case of CMMs, "control" and "flow" devices are aligned and plasma bonded to one another, and assembled devices are subsequently bonded to a cover-slip bottom dishes.

Device functionalization with extra-cellular matrix. To ensure that migrating cells were provided an appropriate extra-cellular matrix surface UCMs and SMMs were coated with

collagen by pipetting 5 µl (of 1 µg /ml) collagen IV solution (Sigma-Aldrich) immediately after plasma bonding. CMM devices were coated with collagen IV by perfusing 10 µg/ml solution of collagen IV through the channels for 1 hour at 37 °C (at 5% CO_2 and ~80% relative humidity) using a syringe pump (Nemesys).

Device preparation. For UCMs and SMMs, after devices were functionalized with collagen, cells were loaded in the central reservoirs and allowed to adhere for 2-3 hours prior to initiating time-lapse imaging. For CMMs, cells were captured in constrictions of the channels and allowed to adhere for 2 hours while keeping a slow perfusive flow (0.5 µl/min). To establish a gradient in the channels, the tubing at the entry of the channels was removed and a syringe containing the media with chemokine was introduced in its place. Flow was then re-started by reactivating the syringe pump and allowing the gradient to balance before beginning acquiring time-lapse data.

MCF7 chemotaxis experiments. MCF7 cells were provided courtesy the Lindquist Lab and were cultured according to standard protocols. Briefly, cells were cultured in DMEM (with L-glutamine) supplemented with 10 % (v/v) fetal bovine serum, and 2% (v/v) penicillin-streptomycin. Cells were split and re-seeded at 1:10 split ratios every 2-3 days. For imaging and visualization, cells were labeled with nuclear-staining Hoechst (Invitrogen) and mitochondrial staining MitoTracker Red (Invitrogen) dyes. After staining, cells were washed twice in 1× PBS and then seeded in UCMs devices for analysis of migration in unconstrained environments. Cells were imaged and mitochondrial localization quantified as in all other experiments described before. Supplementary Figure S3 shows scatter plots of average migration velocity versus MLI, showing that MCF7 cells indeed show localizations similar to MDA-MB-231 cells. Importantly, MCF7 cells show a wide range of persistence and a decreased average velocity compared to MDA-MB-231 cells.

Cell migration in cells with mitochondrial fission and fusion mutations. Mutants overexpressing the fission protein drp-1 and mutants with dominant negative forms of the fusion protein opa-1 show migration and persistence analogous to wildtype migrating cells - Figure S4.

Supplementary Figures

Figure S1: Mutagenesis procedure (A) Genes of interest were obtained in pDONR223 backbones, they were subsequently amplified and sequenced. (B) Genes of interest were then mutagenized, sequenced and amplified. (C) Gateway reactions using LR Clonase II were used to place mutagenized in a CMV-promoter containing backbone (pDEST26). These plasmids were subsequently amplified. (D) Mutagenized (for dominant negative mutants) and non-mutagenized genes (for over-expressing mutants) were co-transfected with an EGFP-containing plasmid using lipid-based transfection reagents. Transfected cells were selected in antibiotic and subsequently single cell cloned.

Figure S2: Quantifying nuclear position in migrating cells. (A) Representative image of MDA-MB-231 breast cancer cell spontaneously migrating through a microchannel. Green arrowhead indicates direction of migration, dashed white lines indicate channel boundaries, and yellow dot indicates centroid of the nucleus. "A" and "P" indicate anterior and posterior regions of the cell. Dashed green line indicates region for corresponding fluorescence line scan (plot). Dashed blue lines indicate cell extents and dashed orange line the midpoint of the cell. Normalized nuclear position is computed from distance between cell extents (E), position of centroid (C), and position of the midpoint of the cell (M). Scale bar 10 μm. (B) Normalized nuclear position is computed for 100 cells from each migration condition described in the main manuscript. Analysis shows only a small variation in nuclear position indicative of negligible bias in the measurements of mitochondrial localization in a moving cell.

Figure S3: MCF7 cell line unconstrained migration in gradients. (A) Scatter plot of average migration velocity versus MLI, showing that MCF7 cells indeed show localizations similar to MDA-MB-231 cells. MCF7 cells show wide range of persistence and decreased average speed compared to MDA-MB-231 cells. These results show statistics for anterior localization indicating that more than half the cells possess this forward localization compared to other localizations. Similar to MDA-MB-231 cells, MCF7 cells show strong correlations between velocity and MLI (blue circles, $r_v = 0.72$) and between persistence and MLI (red circles, $r_p = 0.52$). Linear regression fits for velocity (m=0.58, $R^2 = 0.52$) and persistence (m=0.47, $R^2 = 0.27$) are indicated by blue and red dashed lines, respectively.

Figure S4: Mitochondrial shape dynamics and mutagenesis. Correlations of velocity and persistence with MLI during MDA-MB-231 cancer cell migration. (A) Over-expressing *wildtype* drp-1 enhances fission processes and results in smaller mitochondria. Scatter plots show that cells with this mutation (red circles) behave similar to wildtype cells (blue circles) showing analogous migration velocity and persistence. Migrating $DRP1^{overexp}$ cells show strong correlations between velocity and MLI ($r_v = 0.51$) and persistence and MLI ($r_p = 0.67$). Linear least-squares fits for velocity (left panel, m=0.5, $R^2 = 0.24$) and persistence (right panel, m=0.54, $R^2 = 0.45$) for $DRP1^{overexp}$ cells are indicated by red dashed lines. Wildtype cells also display strong correlations of velocity

(dashed blue line, m=0.63, R^2 = 0.61) and persistence (dashed blue line, m=0.79, R^2 = 0.68) with MLI. (B) Dominant-negative mutations of opa-1 inhibit fusion processes and also result in smaller mitochondria. As in (A), cells with this mutation (red circles) behave similar to wildtype cells (blue circles) showing analogous migration velocity and persistence. Migrating $OPA1^{K301A}$ cells show strong correlations with velocity and MLI (r_v = 0.83) and persistence and MLI (r_p = 0.59). Linear least-squares fits for velocity (left panel, m=0.54, R^2 = 0.69) and persistence (right panel, m=0.41, R^2 = 0.35) are indicated by red dashed lines. Plots and least-squares fits for the wildtype cells (blue circles and blue dashed lines, respectively) are identical to those in (A).

Supplementary Movies

Supplementary Movie SM1. Movie showing MDA-MB-231 cells moving persistently with anterior-localized mitochondria through a 6 × 6 μm channel. Frames were acquired every 15 minutes.

Supplementary Movie SM2. Movie showing one MDA-MB-231 cell moving persistently with anterior-localized mitochondria through a 10 × 6 μm channel. Frames were acquired every 15 minutes.

Supplementary Movie SM3. Movie showing individual MDA-MB-231 cells moving persistently with anterior-localized mitochondria through a 25 × 10 μm channel. Frames were acquired every 15 minutes.

Supplementary Movie SM4. Movie showing a single MDA-MB-231 cell that switches from anterior to posterior localized mitochondria in a micro-scale chamber. Frames were acquired every 15 mins.

Supplementary Movie SM5. Movie showing a single MDA-MB-231 cell navigating a variegated channel. The cell enters with anterior localization and is able to persistently migrate through the 6 × 6 μm center channel. Frames were acquired every 15 mins.

Supplementary Movie SM6. Movie showing a single MDA-MB-231 cell navigating a variegated channel. The cell enters with posterior mitochondria localization, does not migrate persistently, and stops at the entrance of the 6 × 6 μm center channel. Frames were acquired every 15 mins.

Supplementary Movie SM7. Dominant negative mutations of drp-1 ($DRP1^{K38A}$) perturb the distribution of mitochondria and reduce migration velocity and persistence of MDA-MB-231 cells traversing a 6 × 6 μm channel. Frames were acquired every 15 mins.

Supplementary Movie SM8. Over-expression of drp-1 ($DRP1^{overexp}$) has less impact on migration velocity as shown in this movie, showing a representative mutagenized MDA-MB-231 cell with anterior localization successfully traversing a 6 × 6 μm channel. Frames were acquired every 15 mins.

Supplementary Movie SM9. Analogous to drp-1 overexpression, opa-1 dominant negative mutations ($OPA1^{K308A}$) disrupt fusion and result in smaller mitochondria. This movie shows a representative mutagenized cell traversing a 6 × 6 μm channel. Frames were acquired every 15 mins.

Supplementary Movie SM10. Dominant negative drp-1 ($DRP1^{K38A}$) cells with anterior localization of mitochondria move progressively slower through a 6 × 6 μm channel. Frames were acquired every 15 mins.

Supplementary Movie SM11. Analogous to dominant negative drp-1 mutations, opa-1 overexpression ($OPA1^{overexp}$) results in larger mitochondria and adversely affects migration velocity and persistence of MDA-MB-231 cell traversing 6 × 6 μm channels. Frames were acquired every 15 mins.

Supplementary Movie SM12. Related to their inability to re-localize mitochondria, cells with dominant negative mutant forms of drp-1 ($DRP1^{K38A}$) are not able to navigate constraints. This movie shows a cell with anterior-localized mitochondria unable to enter and navigate a 6 × 6 μm constraint. Frames were acquired every 15 mins.

Supplementary Movie SM13. Mitochondrial rhoGTPase (miro-1) knockdown results in cells that have un-localized mitochondrial distribution. This movie shows a cell with miro-1 knockdown which is unable to migrate persistently through a 6 × 6 μm channel. Frames were acquired every 15 mins.

Supplementary Figures

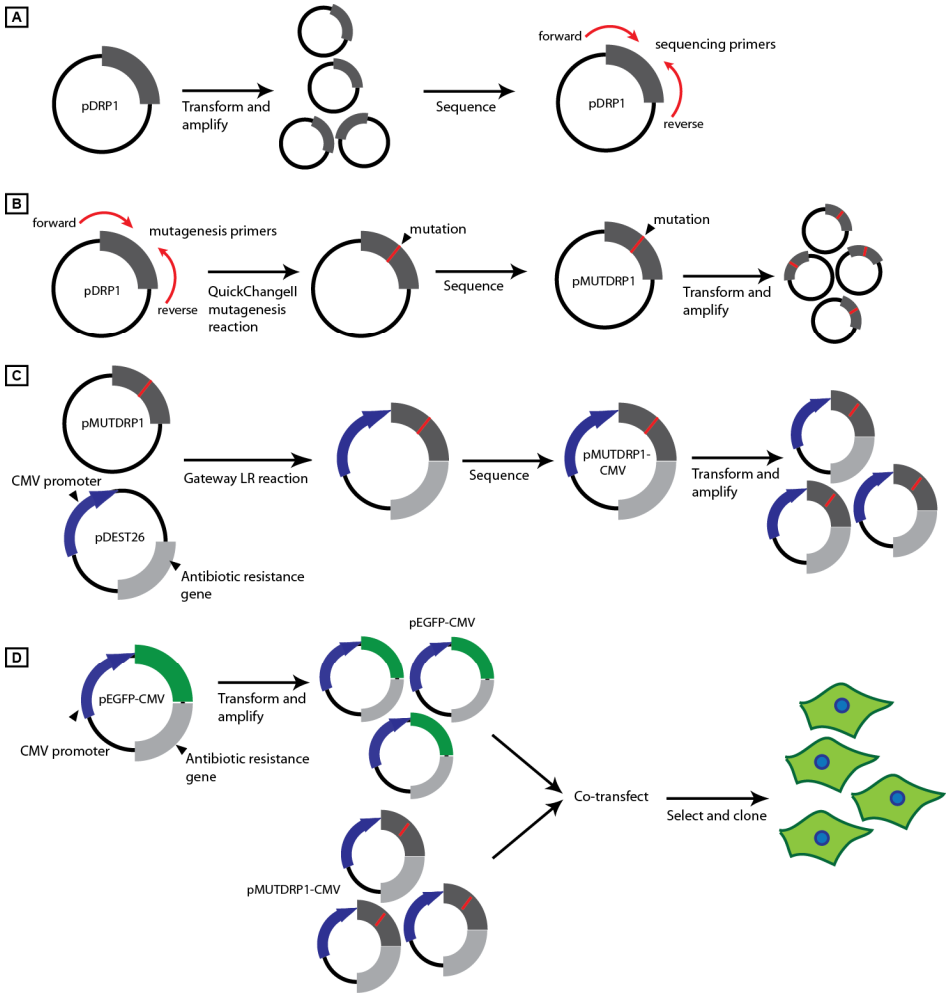

Figure S1

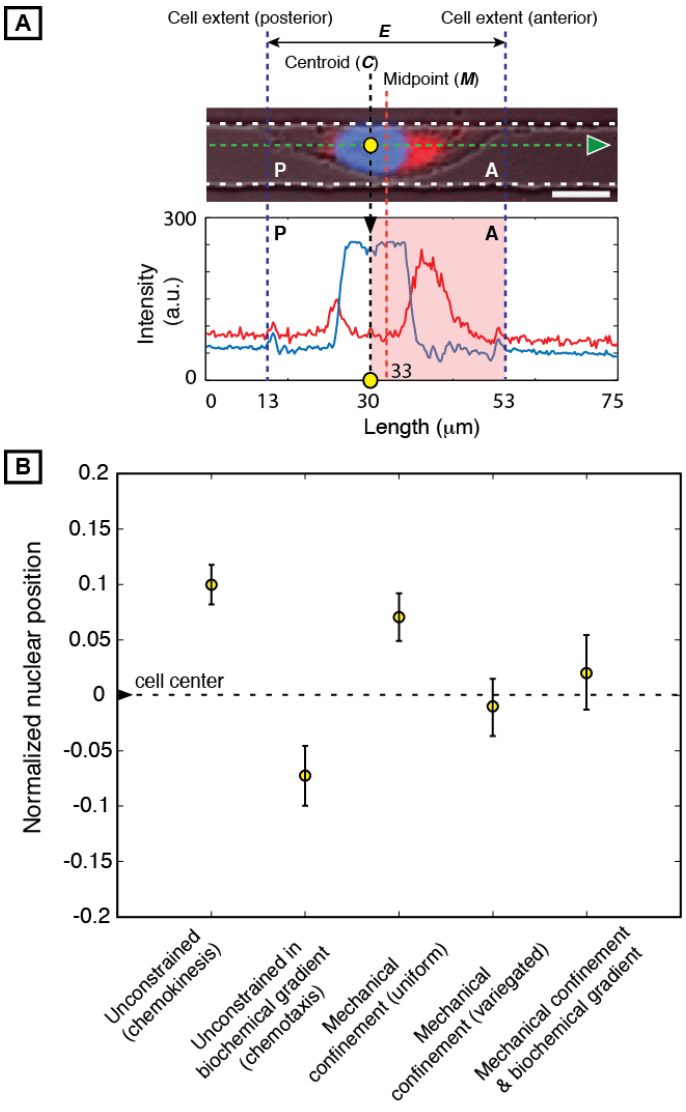
A
Cell extent (posterior)
Cell extent (anterior)
E
Centroid (C)
Midpoint (M)
P
A
300
0
Intensity (a.u.)
33
0
13
30
53
75
Length (μm)
B
0.2
0.15
0.1
0.05
0
-0.05
-0.1
-0.15
-0.2
Normalized nuclear position
cell center
Unconstrained (chemokinesis)
Unconstrained in biochemical gradient (chemotaxis)
Mechanical confinement (uniform)
Mechanical confinement (variegated)
Mechanical confinement & biochemical gradient

Figure S2

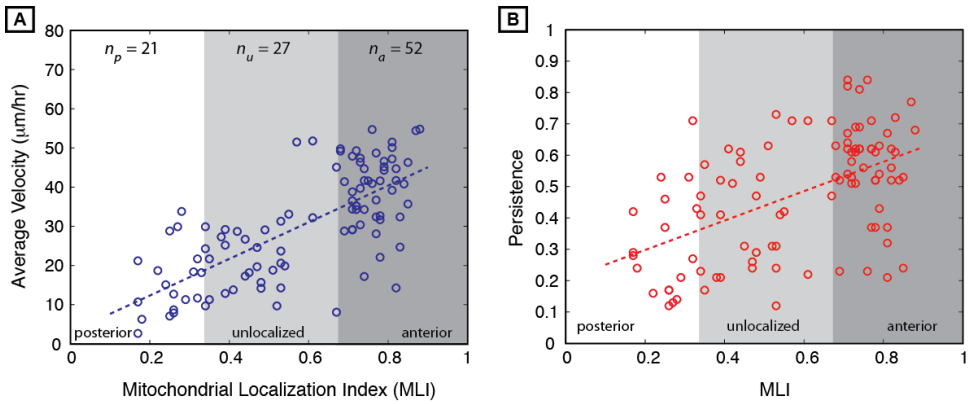
A
B
$n_p = 21$
$n_u = 27$
$n_a = 52$
posterior
unlocalized
anterior
Average Velocity (μm/hr)
Mitochondrial Localization Index (MLI)
Persistence
MLI

Figure S3

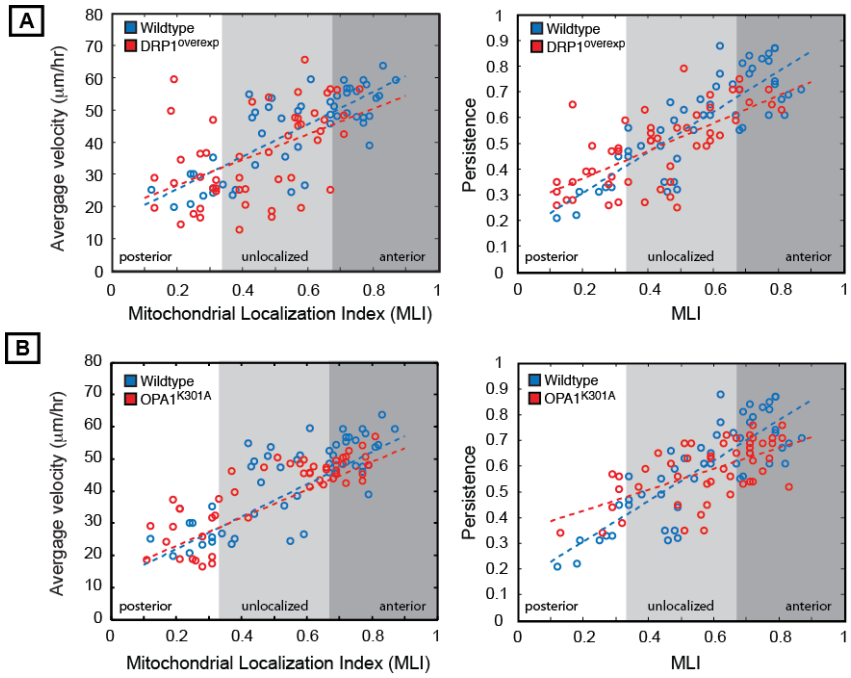
A
Wildtype
DRP1overexp
Avergage velocity (µm/hr)
posterior
unlocalized
anterior
Mitochondrial Localization Index (MLI)
Persistence
MLI
B
Wildtype
OPA1K301A

Figure S4: